

# Ambient Noise Full Waveform Inversion with Neural Operators

Caifeng Zou<sup>1\*</sup>, Zachary E. Ross<sup>1</sup>, Robert W. Clayton<sup>1</sup>,  
Fan-Chi Lin<sup>2</sup>, and Kamyar Azizzadenesheli<sup>3</sup>

<sup>1</sup> *Seismological Laboratory, California Institute of Technology, Pasadena, CA 91125, USA*

<sup>2</sup> *Department of Geology and Geophysics, University of Utah, Salt Lake City, UT 84112, USA*

<sup>3</sup> *Nvidia Corporation, Santa Clara, CA 95051, USA*

## Abstract

Numerical simulations of seismic wave propagation are crucial for investigating velocity structures and improving seismic hazard assessment. However, standard methods such as finite difference or finite element are computationally expensive. Recent studies have shown that a new class of machine learning models, called neural operators, can solve the elastodynamic wave equation orders of magnitude faster than conventional methods. Full waveform inversion is a prime beneficiary of the accelerated simulations. Neural operators, as end-to-end differentiable operators, combined with automatic differentiation, provide an alternative approach to the adjoint-state method. Since neural operators do not involve the Born approximation, when used for full waveform inversion they have the potential to include additional phases and alleviate cycle-skipping problems present in traditional adjoint-state formulations. In this study, we demonstrate the first application of neural operators for full waveform inversion on a real seismic dataset, which consists of several nodal transects collected across the San Gabriel, Chino, and San Bernardino basins in the Los Angeles metropolitan area.

## 1 Introduction

Seismic tomography for sedimentary basins is important for assessing earthquake hazards considering the fact that the basins can trap and amplify seismic waves, leading to stronger and longer ground shaking. Fine-scale subsurface structures are typically determined by active source surveys, which often operate at high frequencies but are expensive and limited by environmental impact issues. Alternatively, seismic data from passive sources, such as ambient noise and earthquakes, can be more readily acquired and can also compensate for the absence of low-frequency information in active source data. It has been shown in seismic interferometry that the cross-correlation between diffuse waveforms recorded at two stations approximates the elastodynamic Green's function (Wapenaar, 2004; Wapenaar et al., 2010). The so-called empirical Green's function (EGF) created from ambient noise is more commonly used by ray theory-based tomography methods (Guo et al., 2015; Lin et al., 2008; Yao et al., 2010; Zheng et al., 2011), which do not account for the finite-frequency effects in heterogeneous media. Full waveform inversion (FWI), which accounts for the full physics of wave

---

\*Corresponding author: czou@caltech.edu

propagation, can reveal more accurate and detailed subsurface structures (Liu et al., 2017, 2023; Maguire et al., 2022; Sager et al., 2020; Wang et al., 2021).

Despite its significant advantages, FWI can be time-consuming and memory-intensive for large problems, which hinders its broader applicability. Moreover, the adjoint-state method (Fichtner et al., 2006a; Liu & Tromp, 2006; Plessix, 2006; Tromp et al., 2005) is conventionally used for FWI, which typically lies within the framework of the Born approximation (Hudson et al., 1977; Miles, 1960; Wu & Aki, 1985). The Born approximation linearizes the relationship between the perturbation to the wavefield and the perturbation to the medium and thus neglects multiple scattering effects, requiring the initial model to be close enough to the true Earth to avoid being trapped in local minima (Gauthier et al., 1986; Fichtner et al., 2006b; Panning et al., 2009; Virieux & Operto, 2009). In ambient noise tomography (ANT), the adjoint method usually requires a model derived from surface wave dispersion analysis and ray-based approximations as a starting point (Chen et al., 2014; Liu et al., 2023; Maguire et al., 2022; Zhang et al., 2018). To tackle these challenges, recent studies have shown that neural operators (Li et al., 2020a,b; Azizzadenesheli et al., 2024) can solve the wave equations orders of magnitude faster than traditional numerical solvers (Yang et al., 2021, 2023; Zou et al., 2024). Using automatic differentiation (AD) (Baydin et al., 2018; Rumelhart et al., 1986) instead of the Born approximation, neural operators have the potential to alleviate, though not fully resolve, the cycle-skipping problem in FWI (Métivier et al., 2018; Pladys et al., 2021; Yao et al., 2019; Sambridge et al., 2022), making it possible to start with a simpler velocity model (e.g., a 1D model).

The primary advantage of neural operators in solving partial differential equations (PDEs) over other prevailing machine learning approaches, such as physics-informed neural networks (PINNs) (Raissi et al., 2019), is that they are trained to learn the solution operator for an entire family of PDEs instead of a specific instance. This means that a neural operator has the potential to generalize to arbitrary PDE coefficients (e.g., velocity structures) if the training instances are ideally sampled, which are commonly sampled from random fields for neural operators. The training is a one-time effort for the forward process and there is no further training for the neural operator in the inversion stage, where the velocity parameters are updated with gradients computed from AD. This is similar to traditional FWI but eliminates the need to generate the adjoint wavefield. This way, we monitor the data misfit and have the flexibility to add regularization as needed.

Our contributions are as follows. We demonstrate the first application of neural operators for ambient noise tomography on a real seismic dataset, specifically the Basin Amplification Seismic Investigation (BASIN) survey (BASIN, 2018; Clayton et al., 2019), which deployed linear nodal arrays in the northern Los Angeles (LA) basins. We provide a trained neural operator that is applicable without retraining to any linear array in the study area, or potentially other problems with a comparable spatial footprint. With the trained neural operator, FWI can be performed two orders of magnitude faster than the conventional adjoint method. Our tomography results are consistent with previous studies in the same region (Ghose et al., 2023; Li et al., 2023; Villa et al., 2023; Zou & Clayton, 2024) without the strong dependence on priors. The proposed method can be scaled to 3D, provided that sufficient computing resources are available.

## 2 Adjoint-State Method with the Born Approximation

Seismic wave propagation in an elastic medium follows the elastic wave equation

$$\rho \frac{\partial^2 \mathbf{u}}{\partial t^2} = \nabla \lambda (\nabla \cdot \mathbf{u}) + \nabla \mu \cdot (\nabla \mathbf{u} + (\nabla \mathbf{u})^T) + (\lambda + 2\mu) \nabla (\nabla \cdot \mathbf{u}) - \mu \nabla \times \nabla \times \mathbf{u} + \mathbf{f}, \quad (1)$$

where  $\mathbf{u}$  is the displacement wavefield,  $\mathbf{f}$  is the body force,  $\rho$  is the density,  $\lambda$  and  $\mu$  are the Lamé parameters. Equation 1 can be restated concisely with an integro-differential operator  $\mathcal{L}$  as

$$\mathcal{L}\mathbf{u} = \mathbf{f}. \quad (2)$$

In seismology the medium is commonly parametrized by P-wave velocity  $V_P$  and S-wave velocity  $V_S$ :

$$V_P = \sqrt{\frac{\lambda + 2\mu}{\rho}} \quad \text{and} \quad V_S = \sqrt{\frac{\mu}{\rho}}. \quad (3)$$

It is assumed that a small perturbation to the medium will perturb the operator  $\mathcal{L}_0$  by  $\delta\mathcal{L}$  and the wavefield  $\mathbf{u}_0$  by  $\delta\mathbf{u}$ . Applying Equation 2 to the perturbed medium results in

$$(\mathcal{L}_0 + \delta\mathcal{L})(\mathbf{u}_0 + \delta\mathbf{u}) = \mathbf{f}. \quad (4)$$

Since  $\mathcal{L}_0\mathbf{u}_0 = \mathbf{f}$ , this leads to

$$\mathcal{L}_0\delta\mathbf{u} + \delta\mathcal{L}\mathbf{u}_0 + \delta\mathcal{L}\delta\mathbf{u} = \mathbf{0}. \quad (5)$$

Neglecting the higher-order term  $\delta\mathcal{L}\delta\mathbf{u}$ , the first-order Born approximation is defined as

$$\mathcal{L}_0\delta\mathbf{u} = -\delta\mathcal{L}\mathbf{u}_0. \quad (6)$$

This indicates that the perturbation to the wavefield can be computed by treating the right-hand side as the source. It also implies that the Born approximation only accommodates single scattering and that it will break down if the perturbation is large relative to the background medium (Panning et al., 2009). Here, FWI is a local optimization strategy, where the solution is sought in the vicinity of an initial model by minimizing an objective function  $\Phi$ :

$$\Phi = \frac{1}{2} \|\mathbf{u}_r - \mathbf{d}\|_2^2 \quad \text{where} \quad \mathbf{u}_r = \mathbf{R}\mathbf{u}, \quad (7)$$

where  $\mathbf{u}_r$  is the simulated waveforms queried at receivers through a sampling operator  $\mathbf{R}$ , and  $\mathbf{d}$  is the observed data. Based on the Born approximation, the gradients of the objective with respect to parameters of interest  $\mathbf{m}$  can be estimated as the cross-correlation between the forward wavefield  $\mathbf{u}$  and the adjoint wavefield  $\mathbf{v}$  at zero time lag (Louboutin et al., 2019):

$$\nabla_{\mathbf{m}}\Phi = \sum_{i=1}^{N_t} \mathbf{u}[i] \mathbf{v}_{tt}[i], \quad (8)$$

where  $N_t$  is the number of time steps and the subscript  $tt$  denotes a second-order time derivative. Equation 8 defines the adjoint-state method, in which the adjoint wavefield  $\mathbf{v}$  is generated by back-propagating the residual  $\delta\mathbf{d}$  in the medium:

$$\mathcal{L}\mathbf{v} = \mathbf{R}^T \delta\mathbf{d} \quad \text{where} \quad \delta\mathbf{d} = \mathbf{u}_r - \mathbf{d}. \quad (9)$$

In summary, the adjoint-state method with the Born approximation requires the initial model to be sufficiently accurate, with a travel-time error of less than half the period (Beydoun & Tarantola, 1988; Virieux & Operto, 2009). Otherwise, the cycle-skipping phenomenon may arise, leading to convergence to a local minimum (Gauthier et al., 1986; Pladys et al., 2021).

### 3 Methods

#### 3.1 Helmholtz Neural Operator with Automatic Differentiation

The Green’s function  $G$  is the impulse response of a linear differential operator  $\mathcal{L}$  defined on a bounded, open domain  $D \subset \mathbb{R}^d$  with specified parameters  $a$ :

$$\mathcal{L}G_a(x, s) = \delta(x - s) \quad \text{where } x \in D, \tag{10}$$

where  $\delta$  is the Dirac delta function and  $s$  is the location of a point source. The solution to Equation 2 can then be derived from

$$u(x) = \int_D G_a(x, y) f(y) dy, \tag{11}$$

where  $f$  refers to the source function. This describes a linear mapping from  $f$  to  $u$  provided that  $a$  (e.g., velocity) is fixed. However, in seismic wave propagation, the direct mapping from  $a$  to  $u$  is nonlinear and unknown in closed form. Based on the universal approximation theorem, neural operators can approximate arbitrary nonlinear continuous operators (Hornik et al., 1989; Kovachki et al., 2023).

The solution operator can be parameterized much more efficiently in memory when solving Equation 2 in the frequency domain (i.e., the Helmholtz equation) than in the time domain, for which the Helmholtz Neural Operator (HNO) was proposed by Zou et al. (2024). This is because different frequency components can be solved individually and, thus, parallelized. Solutions in the time and frequency domains can be combined via the (inverse) Fourier transform. In this study, we construct a U-shaped HNO comprising  $L = 8$  inner layers of Fourier Neural Operators (FNOs) (Li et al., 2020a) to approximate the solution operator for the elastic wave propagation:

$$\begin{aligned} v_0(x) &= (\mathcal{P} a)(x), \\ v_{l+1}(x) &= \sigma(\mathcal{W}_l v_l(x) + \mathcal{F}^{-1}(\mathcal{F}(\kappa_l) \cdot \mathcal{F}(v_l))), \\ u(x) &= (\mathcal{Q} v_L)(x), l = 0, \dots, L - 1, \end{aligned} \tag{12}$$

where  $a$  is the input including  $V_P$ ,  $V_S$ , the source location, and a constant function indicating the frequency value,  $u$  is the output wavefield solution,  $v_l$  is input to the  $l + 1^{th}$  layer,  $\mathcal{P}$  is a point-wise operator used to lift the dimension,  $\mathcal{Q}$  is used to project the output to the desired dimension,  $\mathcal{W}_l$  acts as a residual connection,  $\kappa_l$  is a parametric kernel function,  $\mathcal{F}$  and  $\mathcal{F}^{-1}$  denote the Fourier transform and inverse Fourier transform, respectively, and  $\sigma$  is a nonlinear activation function, which we set as GELU (Hendrycks & Gimpel, 2016). Figure 1 illustrates the model architecture and Table S1 provides the details in each FNO layer. We use FNOs to speed up the integral calculation, and the U-shape allows for a deeper model and skip connections (Li et al., 2020c; Rahman et al., 2022; Ronneberger et al., 2015).

In the previous section, we showed that in the conventional adjoint method, the gradients for updating velocity parameters are computed based on the Born approximation. However, with neural operators (or other machine learning methods developed in the PyTorch framework), the gradients of the objective to any parameters in the computational graph are automatically computed using the chain rule (Rumelhart et al., 1986). For example, if the scalar-valued objective function  $J$  is defined as

$$J = \frac{1}{2} \sum_{i=1}^N (\hat{u}_i - u_i)^2, \tag{13}$$

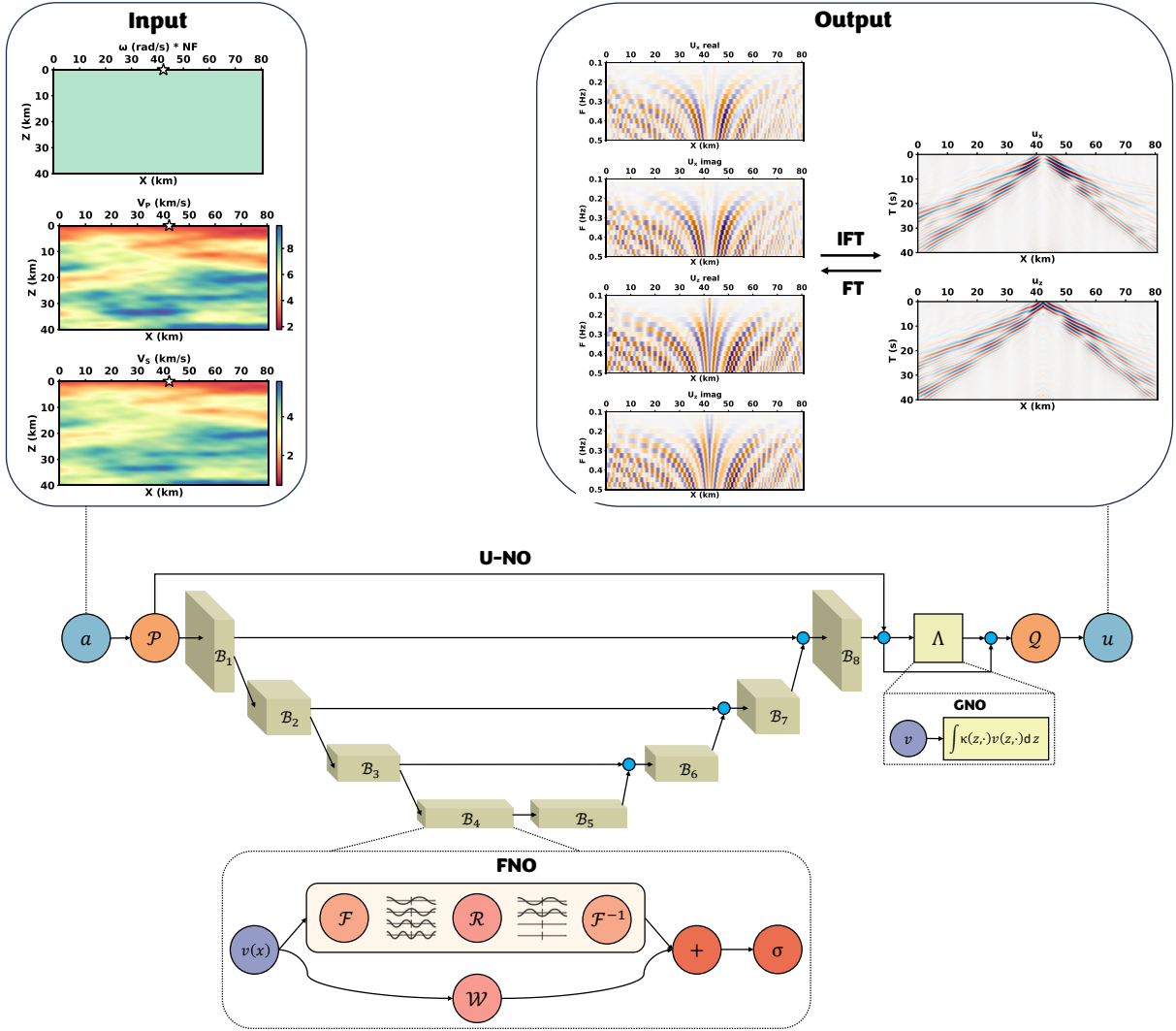


Figure 1: Model architecture.  $a$  is the input including  $V_P$ ,  $V_S$ , the source location, and a constant function indicating the frequency value.  $u$  is the output wavefield solution.  $\mathcal{P}$  is a point-wise operator used to lift the dimension.  $\mathcal{Q}$  is used to project the output to the desired dimension.  $\mathcal{B}$  is the inner integral operator chosen as the FNO, in which  $v$  is input to the layer,  $\mathcal{F}$  and  $\mathcal{F}^{-1}$  denote the Fourier transform and inverse Fourier transform, respectively,  $\mathcal{R}$  is a linear operator,  $\mathcal{W}$  acts as a residual connection, and  $\sigma$  is a nonlinear activation function.  $\Lambda$  is a graph neural operator (GNO) used to query the waveforms at the free surface, which is parameterized as a neural network with (96, 96, 96) neurons.

where  $N$  is the number of observations,  $\hat{u}_i$  is the model prediction, and  $u_i$  is the ground truth, the gradient of  $J$  with respect to a parameter  $m_j$  is given by

$$\frac{\partial J}{\partial m_j} = \sum_{i=1}^N \frac{\partial J}{\partial (\hat{u}_i - u_i)} \frac{\partial (\hat{u}_i - u_i)}{\partial \hat{u}_i} \frac{\partial \hat{u}_i}{\partial m_j} = \sum_{i=1}^N (\hat{u}_i - u_i) \frac{\partial \hat{u}_i}{\partial m_j}, \quad (14)$$

where  $\frac{\partial \hat{u}_i}{\partial m_j}$  is further derived through a chain of differential operations. This is termed the reverse-mode AD (Baydin et al., 2018; Elliott, 2018). Because all the functions, expressions, and control flow structures used in neural operators are differentiable and compatible with AD, it is unnecessary to run an adjoint simulation for gradient estimation. Furthermore, the linearization taken by the Born approximation is not made here, which will ease the need for close initial models. Note that this does not mean the HNO-AD method is independent of initial models, but rather that it only reduces the dependence. It is still likely to get stuck in local minima due to bad initialization.

### 3.2 Data-Driven Training

In this study, we train a single 2D HNO for linear nodal arrays across the northern LA basins. The model is trained in a supervised learning manner and with synthetic data generated from a spectral element method (SEM) using the software SALVUS (Afanasiev et al., 2019). The computational domain is set to 80 km (horizontal)  $\times$  40 km (vertical) on a  $256 \times 128$  mesh, which accommodates the longest seismic line in the area. We simulate 40-s-duration wavefields with a time step of 0.001 s, which are excited by a vertical force and Ricker wavelet time function with a central frequency of 0.3 Hz. For ambient noise data applications, the source is randomly placed along the free surface from a uniform distribution of horizontal position. The  $V_P$  and  $V_S$  models are generated from random fields, the parameters of which are provided in Table S2. The density models are derived from  $V_P$  using the empirical relation by Brocher (2005), which are input to SALVUS but not to the HNO. The time-domain solutions from the SEM solver are Fourier-transformed and filtered to the frequency band of interest (0.1 to 0.5 Hz) for use with the HNO. We train an HNO using 27000 simulations and validate the model performance using 3000 simulations (where a simulation means a single source and a particular velocity model). We define the loss function as

$$Loss = 0.95 \frac{\|\mathbf{u} - \hat{\mathbf{u}}\|_1}{\|\mathbf{u}\|_1} + 0.05 \frac{\|\mathbf{u} - \hat{\mathbf{u}}\|_2}{\|\mathbf{u}\|_2}, \quad (15)$$

where  $\mathbf{u}$  and  $\hat{\mathbf{u}}$  denote the true and predicted wavefields, respectively. We use an Adam optimizer (Kingma & Ba, 2014) with a learning rate of 0.001 and a scheduler that decays the learning rate by half every 30 epochs. The batch size is 256. Figure S1 shows the loss curves. The full training process took 2 days with 8 NVIDIA RTX A6000 GPUs. Note that the training is a one-time effort and no further training is required for different seismic lines or the inversion stage. Table 1 compares the time consumed by SALVUS and the trained HNO in forward modeling and FWI under the same configuration. In performing FWI for this 2D case, the HNO with AD is approximately two orders of magnitude faster than the SEM with the adjoint method. The computational advantage will only be greater in 3D (Zou et al., 2024).

### 3.3 Synthetic Tests

To test generalization, we first evaluate the HNO performance with the synthetic data generated from a community velocity model named CVM-S4.26 (Lee et al., 2014). We extract a profile of

Table 1: Comparison of time consumed by SALVUS and HNO in forward modeling and FWI. The experiments are conducted on a community model called CVM-S4.26 using a single NVIDIA RTX A6000 GPU. The forward modeling time is measured for a single event with one source and 234 receivers on the free surface. The FWI time is measured for one tomographic iteration for the same event configuration.

	SALVUS	HNO
Forward modeling	7.18 s	0.18 s
FWI	128.51 s	0.45 s

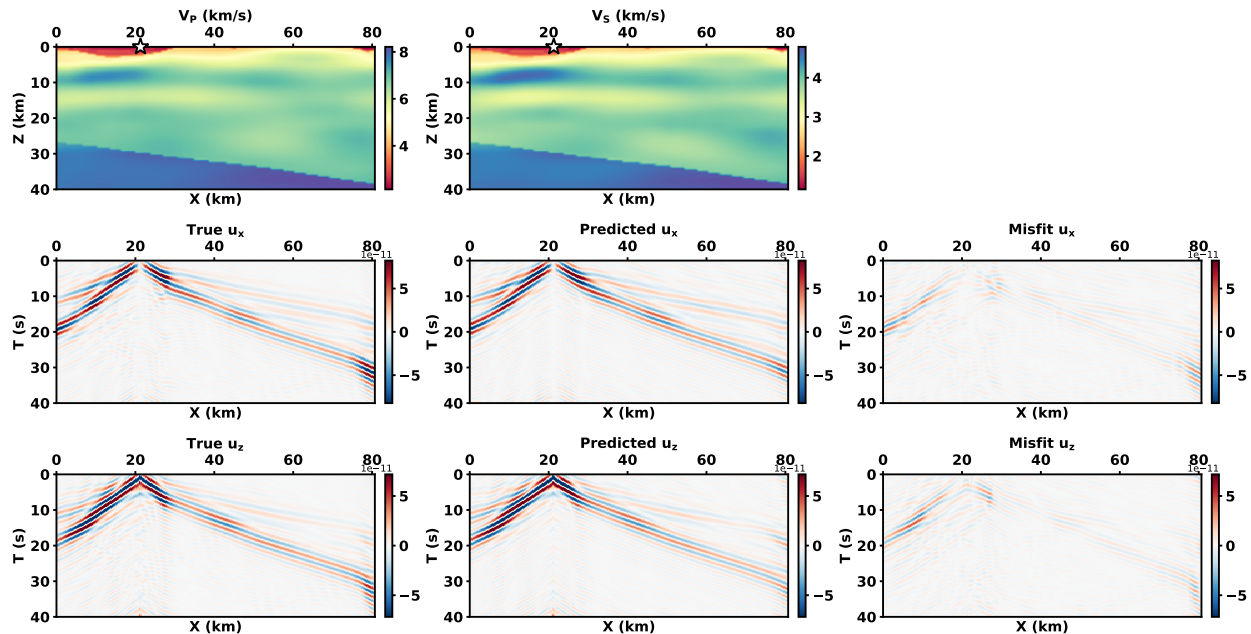


Figure 2: Comparing simulations for velocity model CVM-S4.26 between HNO and baseline method. Source location is marked by a white star.

the 3D CVM-S4.26 along the longest seismic line, SB1, in the BASIN survey. Figure 2 shows the HNO-predicted results for a sample shot, with the SALVUS-simulated waveforms serving as the ground truth. The direct output of the HNO is in the frequency domain and is Fourier-transformed to the time domain for visualization purposes. The forward prediction by the HNO is not perfect with a cross-correlation coefficient of 0.98, but we will show that it is sufficiently accurate in the upcoming FWI experiment.

Before the inversion, we compute the sensitivity kernels for the HNO-AD method (Equation 14), following the definition in Tromp et al. (2005). In Figure 3, we put sources and receivers at nodes on the free surface and sum the gradients of the misfit with respect to the velocity parameters over all source-receiver pairs. The misfit is defined as the squared error between the HNO-predicted wavefield with a 1D initial model and the SALVUS-simulated wavefield with the true model (CVM-S4.26). We average the sensitivity kernels horizontally to obtain functions of depth. It can be seen that the sensitivity drops dramatically with depth, which indicates that updates to deeper parts of the

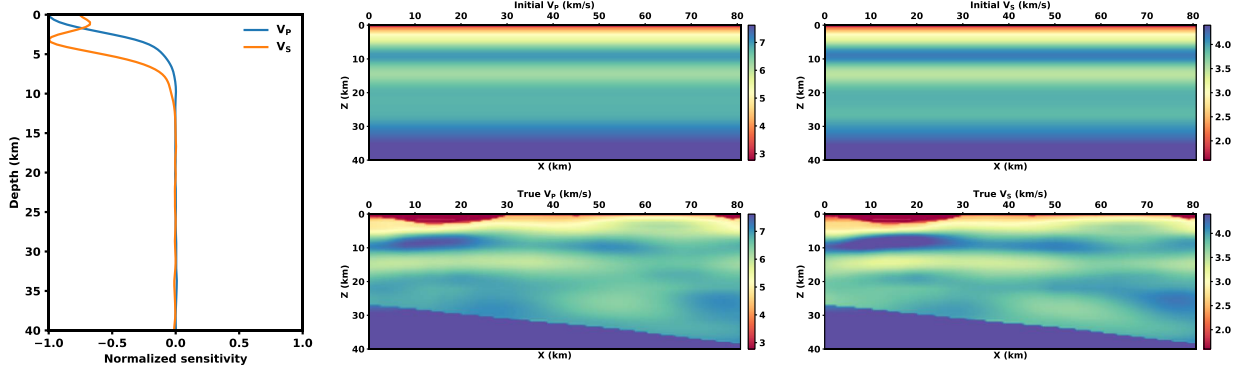


Figure 3: Sensitivity kernels for the HNO-AD method, defined as the gradients of the misfit with respect to the velocity parameters, which are summed over all source-receiver pairs and averaged horizontally. The misfit is defined as the squared error between the HNO-predicted wavefield with a 1D initial model and the SALVUS-simulated wavefield with the true model (CVM-S4.26). The sensitivity values for  $V_P$  and  $V_S$  are each normalized by its maximum amplitude.

velocity models are less reliable. Therefore, we will only present the inversion results for the top 10 km hereafter.

In the inversion stage, we freeze the HNO parameters and update  $V_P$  and  $V_S$  simultaneously with gradients calculated from AD. The inversion is also performed in the frequency domain, and the objective function is defined as the mean squared error (MSE) between the HNO-predicted and SALVUS-simulated wavefields. For use with ambient noise data where the amplitude is often not well-defined, we normalize the amplitude to unity before computing the MSE. We add no regularization term to the objective function but implicitly impose some regularization by smoothing the gradients with a Gaussian filter (Tape et al., 2010; Zhu et al., 2015). The smoothing radius is set to  $3 \times$  grid spacing (945 m). We average the CVM-S4.26 profile horizontally to get a 1D initial model. We start with lower frequency data and gradually feed in higher frequency components, which is also common practice in traditional FWI (Wang et al., 2018; Zhang et al., 2018). This is because lower frequency data are usually less noisy, easier to fit, and better for global convergence. Also, the neural operator performs more accurately for lower frequencies (Zou et al., 2024).

We also use an Adam optimizer for gradient descent in FWI, with a learning rate of 0.05 and a scheduler that decays the learning rate by half every 5 epochs. The gradients are summed over a mini-batch of 64 data points, where a single data point corresponds to a single frequency and a single source. We monitor MSE for the full frequency band while progressively incorporating higher frequency data as inversion proceeds, as shown in Figure 4. We conduct FWI experiments on both noise-free data and data perturbed with different levels of Gaussian random noise. We activate 234 sources along the free surface of the CVM-S4.26 slice for SB1, located at the nodes. The receivers are also placed at the nodes.

Figure 5 shows a sample shot of synthetic data perturbed with different levels of noise. The noise is generated from a zero-mean Gaussian distribution with a standard deviation (SD) equal to a factor times the SD of the noise-free data. The corresponding FWI results for noise-free data and noisy data are displayed in Figure 6. The noise-free inversion in the second row clearly reveals the basin

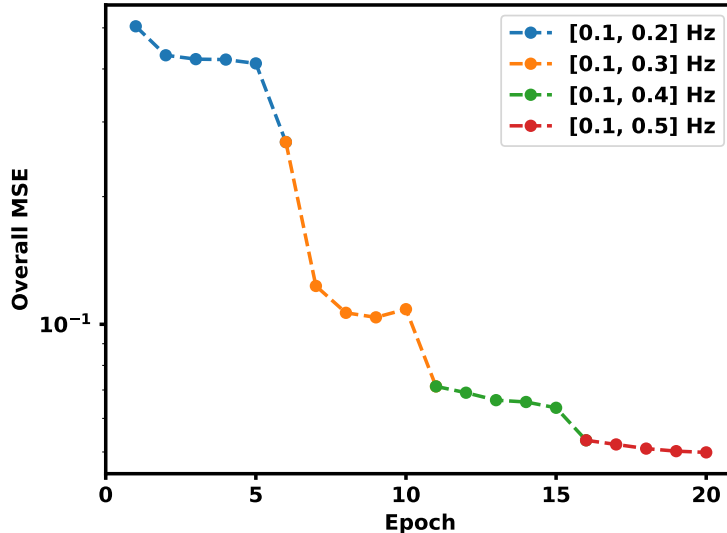


Figure 4: Overall MSE (mean squared error) in the FWI process, where higher frequency data is progressively incorporated. We use an Adam optimizer with a learning rate of 0.05 and a scheduler that decays the learning rate by half every 5 epochs. The batch size is 64.

model, demonstrating the forward modeling accuracy of the HNO from another perspective. The deeper part of the model is not well resolved because the source-receiver geometry limits sensitivity to near-surface regions. When  $5\times$  noise is added, the FWI results maintain good quality, even though the seismic signal already becomes unrecognizable to the eye. We increase the noise level until the inversion is on the verge of collapse, with a perturbation of  $10\times$  noise that totally obliterates the waveforms.

These synthetic tests serve to verify the generalizability of the neural operator trained with random fields and noise-free data to realistic velocity structures and noisy data, supervised by some definition of ground truth that is unavailable in real data. They show the excellent performance of the HNO-AD method in low signal-to-noise ratio (SNR) situations. Additionally, the entire FWI process can be completed in minutes. In contrast, FWI with the adjoint-state method takes 16 hours for 10 iterations and makes little progress with the same 1D initialization even for noise-free data (Figure S2).

### 3.4 Application to Real Seismic Data from the Broader Los Angeles Region

We apply the trained neural operator to a real-world ambient noise tomography example. The real data comes from the BASIN survey that deployed 10 linear nodal arrays in the San Gabriel (SG), Chino, and San Bernardino (SB) basins north of LA (Clayton et al., 2019). 758 Fairfield ZLand three-component nodes with a corner frequency of 5 Hz recorded ambient noise for approximately a month. The spacing ranges from 250 to 300 m. Figure 7 shows a map of the study area and station configuration. The sedimentary formations date from the opening of the LA basin in the Miocene (Wright, 1991). Details in the geologic setting can be found in Villa et al. (2023) and Ghose et al. (2023).

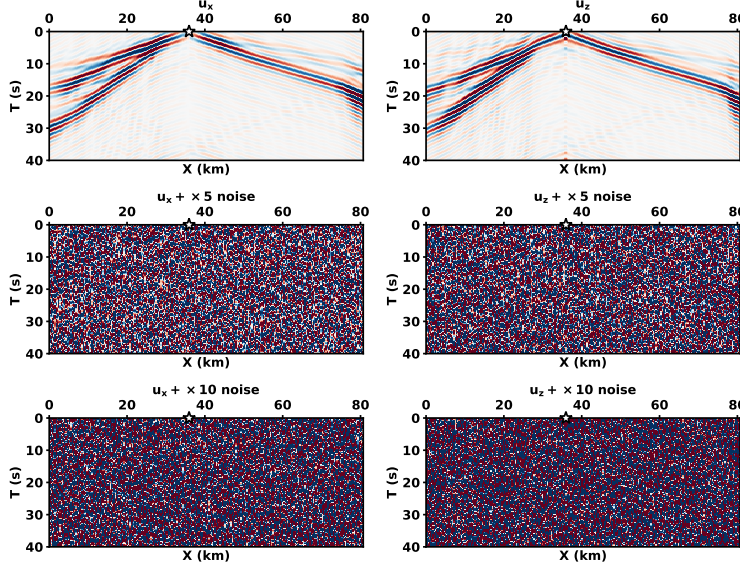


Figure 5: A sample shot of synthetic data perturbed with different levels of noise. The noise is generated from a zero-mean Gaussian distribution with a SD equal to a factor times the SD of the noise-free data.

We take the EGF derived from ambient noise cross-correlation as the direct observation:

$$G_{AB}(t) = -\frac{d}{dt} \left( \frac{C_{AB}(t) + C_{AB}(-t)}{2} \right) \quad \text{where } t > 0, \quad (16)$$

where  $G_{AB}(t)$  is the displacement EGF between two stations  $A$  and  $B$ , and  $C_{AB}(t)$  is the cross-correlation between the seismograms recorded at these two stations. The positive and negative lags of  $C_{AB}$  are averaged to enhance the SNR and to mitigate the effect of inhomogeneous source distribution (Lin et al., 2008). Our cross-correlation workflow is based on Bensen et al. (2007). Equation 16 is indeed a far-field approximation, which holds for inter-station distance greater than three wavelengths (Yao et al., 2006). However, in practice, this condition is often relaxed to make better use of the available data (Li et al., 2023; Wu et al., 2021; Zhang et al., 2018). Especially for a local-scale survey like BASIN, we set the minimum inter-station distance to 5 km for use with 0.2 to 0.5 Hz data. Increasing this distance to 10 km yields a very similar result (Figure S3).

The EGF obtained from cross-correlation accounts for wave physics in a 3D medium, to which a phase shift of  $\pi/4$  must be applied prior to a 2D inversion (Forbriger et al., 2014; Schäfer et al., 2014; Zhang et al., 2018). Figure S4 shows the effect of this transformation. A factor for amplitude correction is further needed, but we only use the phase information, as the amplitude recovered in ANT is not well-defined due to various normalizations done in data processing (Bensen et al., 2007). We have verified through synthetic tests that the phase information is sufficient to reconstruct the velocity models (Figure 6). We focus solely on the phase information by normalizing the amplitude to unity in inversion. This helps to bridge the gap between the synthetic Green's function (SGF) and EGF, as they have different source bandwidths. We match the Z-Z and Z-R cross-correlations with the vertical and horizontal wavefield components predicted by the HNO, respectively. While we mainly retrieve Rayleigh waves with particle motion confined in a 2D plane, we will also discuss the

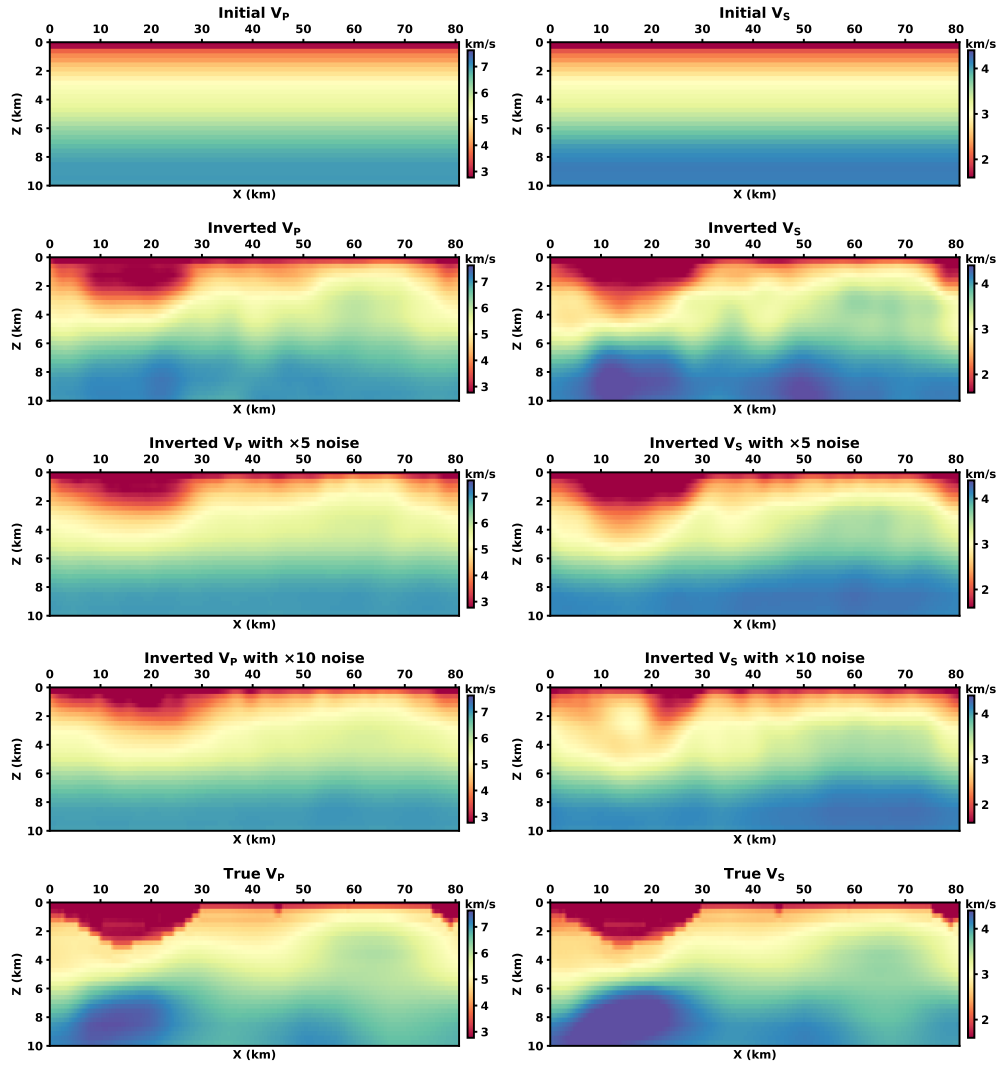


Figure 6: Synthetic FWI results for noise-free data and noisy data.

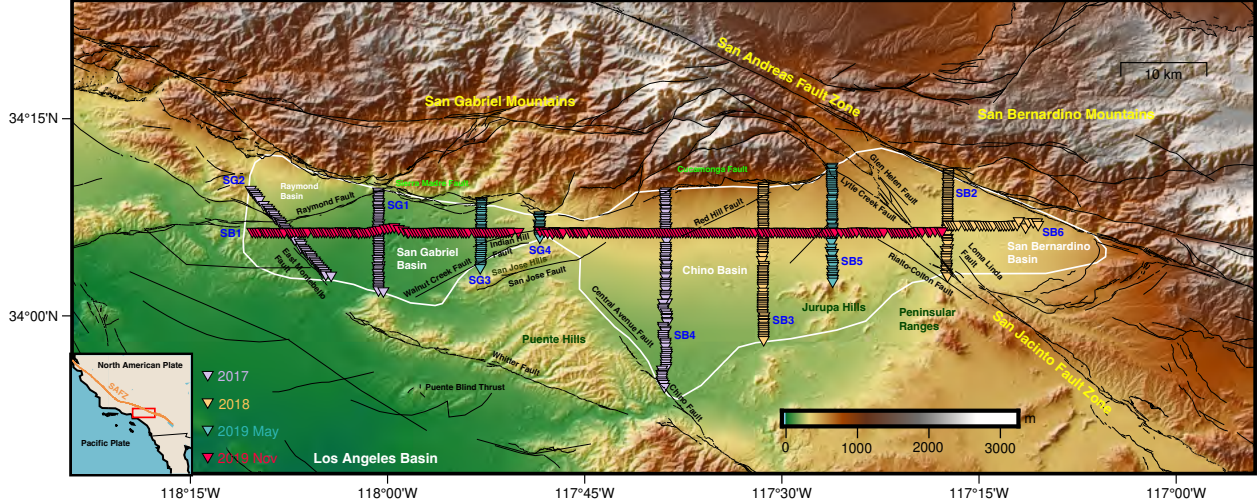


Figure 7: Map of the northern Los Angeles basins, adapted from Zou & Clayton (2024). The study region is outlined by the white polygon. Triangles in different colors show nodal lines deployed in different time periods.

use of Love waves through T-T correlations for the 2D anti-plane problem in the next section. In this study, we follow the principle of Green’s function retrieval, while Tromp et al. (2010), Sager et al. (2018, 2020), and Tsai et al. (2024) established the full waveform ambient noise inversion technique that goes beyond that by interpreting correlation functions as self-consistent observables.

We maintain most settings from the previous synthetic FWI results in carrying out the real data experiments, except we include an additional regularization term that encourages the inverted  $V_P$  and  $V_S$  to respect Brocher (2005):

$$L_{reg} = \frac{1}{M} \sum_{i=1}^M (V_{P_i} - (0.9409 + 2.0947V_{S_i} - 0.8206V_{S_i}^2 + 0.2683V_{S_i}^3 - 0.0251V_{S_i}^4))^2, \quad (17)$$

where  $M$  is the number of grid points on which the velocity models are discretized.

## 4 Results

### 4.1 San Gabriel and Chino Basins

We begin the real data FWI with the longest line, SB1, which extends about 80 km from west to east. Beneath SB1 lie two significant basins — the deeper SG basin in the west and the shallower Chino basin in the east. The depth of the sediment-basement interface has been constrained by Villa et al. (2023). In addition to this 3D basin depth model and the CVM-S4.26 (Lee et al., 2014), another reference is from Li et al. (2023) who constructed a 3D shear wave velocity model for the same area through surface wave dispersion analysis. We start the inversion with a 1D model calculated from this reference model, which results in Figure 8a. Overall, the inverted velocity models reveal basin structures that align well with Villa et al. (2023), capturing significant features including the deeper and more heterogeneous SG basin in the west and the low-velocity zone at the edge of the relatively

flat Chino basin adjacent to the SB basin. We demonstrate the robustness of this result through another two initial models, the smoothed models from Li et al. (2023) (Figure 8b) and CVM-S4.26 (Figure 8c). Results from these different initial models show excellent overall consistency, although they differ in details. In particular, the 1D initial model can achieve performance comparable to that of models with more detailed priors.

The incorporation of higher frequency data in later stages of FWI contributes to refining the shallower structure but also introduces high-frequency noise. Meanwhile, the inaccuracy of the neural operator in forward modeling introduces another source of uncertainty. We compare SALVUS-simulated waveforms (SGFs) using the CVM-S4.26, model from Li et al. (2023), and our model from Figure 8a with the EGF for SB1 in Figure 9. The corresponding waveform difference is plotted in Figure S5. The point here is not to conclude that our model is better than others, as we have not incorporated the full wave physics in 3D, but rather to demonstrate that the HNO-AD method can achieve accuracy comparable to traditional methods at a much lower cost in terms of time and effort. Also note that our model starts with a 1D initial model, while the other two models have stronger priors (Lee et al., 2014; Li et al., 2023).

The same neural operator can be directly applied to any seismic line in the study region. We show another two examples for SB4 and SG1 in Figures 10 and 11, respectively. For SB4 that crossed the Chino basin from north to south, our inversion result reveals a low-velocity zone at the southern end near the Chino fault (Figure 7), which is also seen in the CVM-S4.26 and Li et al. (2023). The low-velocity anomalies between 0 and 15 km present in Li et al. (2023) are absent in both our model and CVM-S4.26. While the authors did not provide specific interpretation, the seismic line crossed the Red Hill fault at approximately 5 km, which could explain the observed discontinuity (if it is not an artifact). Interestingly, our model shows a velocity jump near the Red Hill fault. Overall, the tomography for SB4 displays a shallow (approximately 2 km) sedimentary basin in agreement with previous studies. The sediment-basement interface beneath SG1 is much deeper, as captured in all the displayed models. Our result for SG1 aligns with that for SB1 in the SG basin in terms of basin depth but captures less heterogeneity, which might be limited by the array length. These plug-and-play inversions can be completed in a few minutes.

## 4.2 Use of Love Waves from T-T Correlations

In previous sections, we focused on the 2D in-plane problem (Equation 1) associated with Rayleigh waves and inverted for  $V_P$  and  $V_{SV}$  models. The  $V_{SH}$  model can be separately derived from Love waves with particle motion perpendicular to the plane through T-T cross-correlations  $u_T$ , which is termed the anti-plane problem:

$$\frac{1}{\rho V_{SH}^2} \frac{\partial^2 u_T}{\partial t^2} - \nabla \cdot \left( \frac{1}{\rho} \nabla u_T \right) = f. \quad (18)$$

In this section, we invert for the  $V_{SH}$  model for SB1 following the same methodology to complete the 2D FWI.  $V_{SV} = V_{SH}$  only holds when the medium is isotropic. We define the radial anisotropy as in Jaxbyulatov et al. (2014):

$$\xi = \frac{2(V_{SH} - V_{SV})}{V_{SH} + V_{SV}}. \quad (19)$$

Figure 12 compares the inverted  $V_{SV}$  and  $V_{SH}$  models for SB1 and plots the radial anisotropy. The same 1D initial model as in Figure 8a is used for both cases and we take the relatively robust

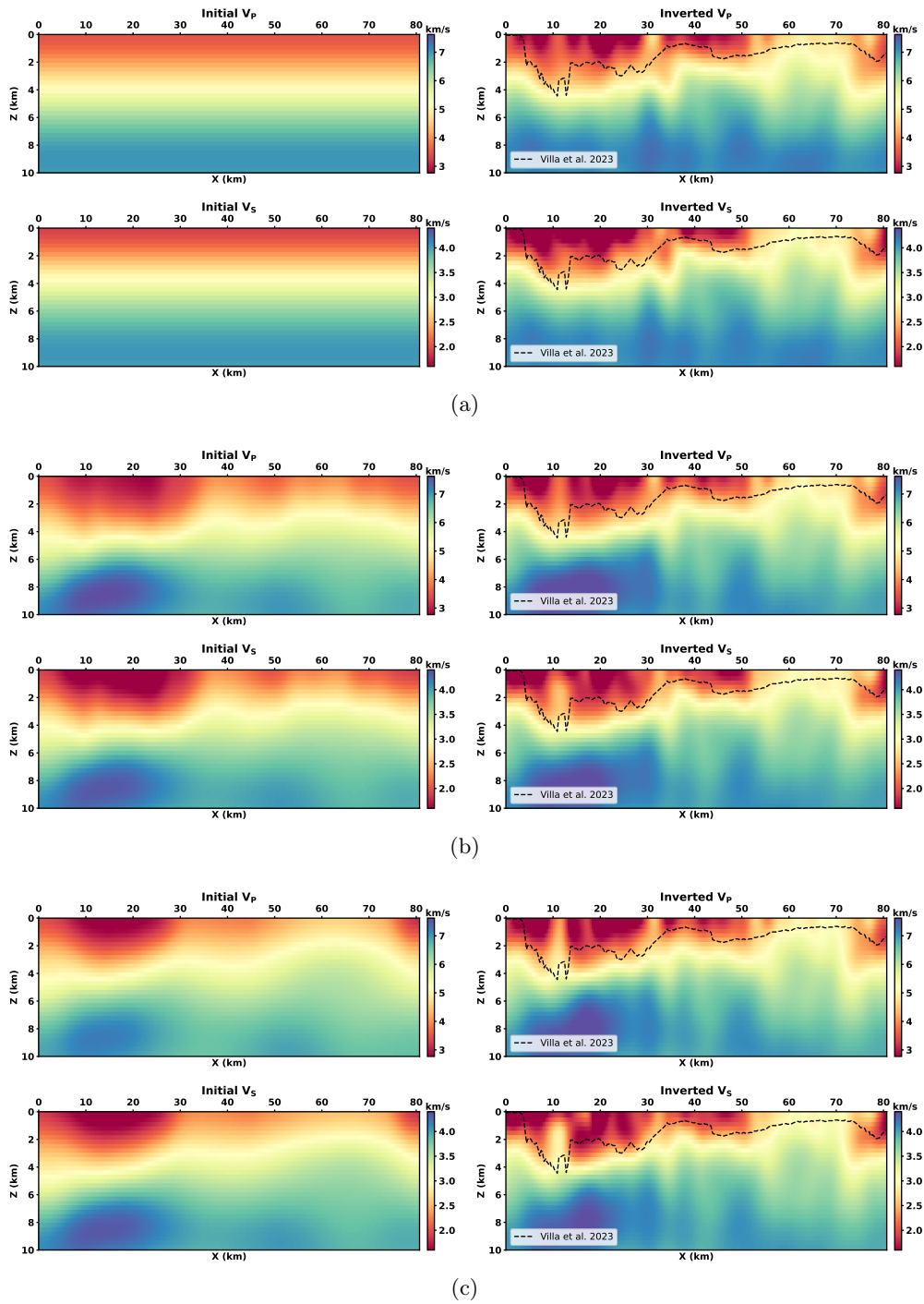


Figure 8: Inversion results for SB1 with different initial models including the (a) 1D and (b) smoothed models from Li et al. (2023), and (c) the smoothed CVM-S4.26. The along-profile distance increases from west to east. The basin bottom from Villa et al. (2023) is delineated with black dashed lines for reference.

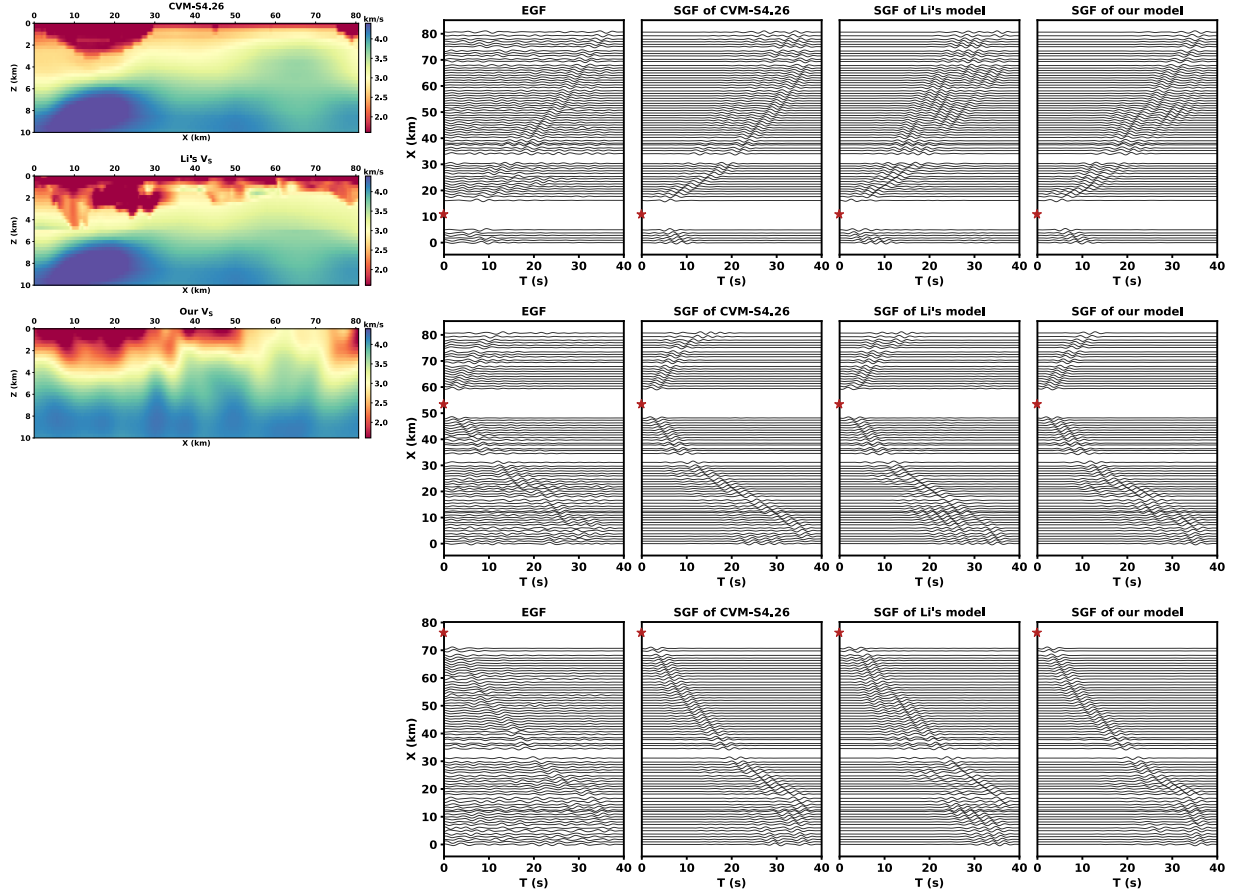


Figure 9: Examples of SALVUS-simulated waveforms (SGFs) using the CVM-S4.26, model from Li et al. (2023), and our model from Figure 8a compared with the EGF for SB1. Only  $V_S$  is plotted for simplicity. The frequency band of the data is 0.2 to 0.5 Hz. In plotting, the waveform is normalized by trace and every third trace is displayed.

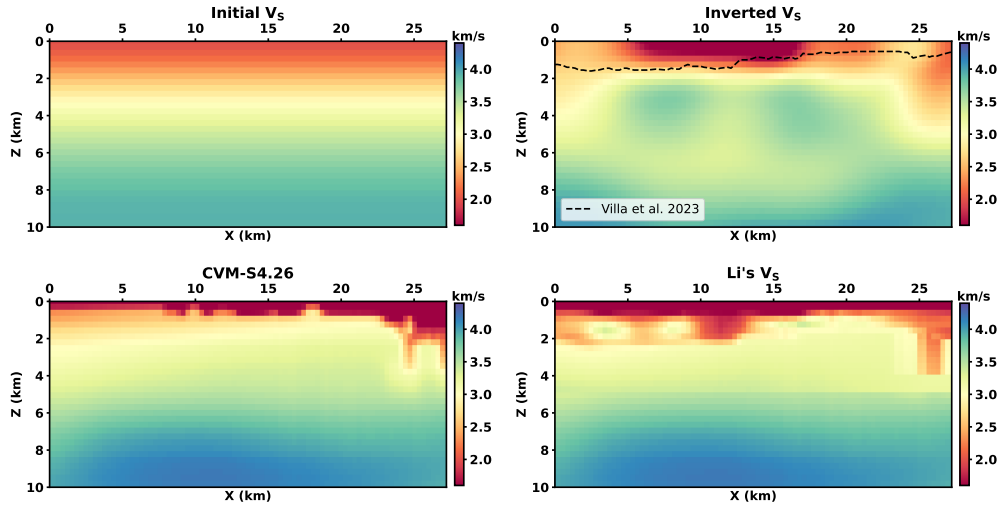


Figure 10: Inversion results for SB4, in comparison to the CVM-S4.26 and model from Li et al. (2023). Only  $V_S$  is plotted for simplicity. The along-profile distance increases from north to south. The basin bottom from Villa et al. (2023) is delineated with black dashed lines for reference.

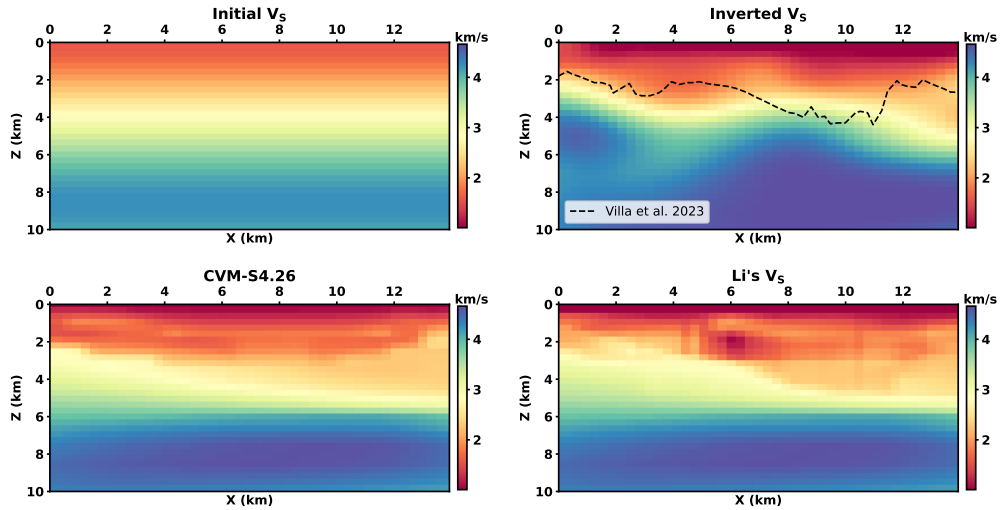


Figure 11: Inversion results for SG1, in comparison to the CVM-S4.26 and model from Li et al. (2023). Only  $V_S$  is plotted for simplicity. The along-profile distance increases from north to south. The basin bottom from Villa et al. (2023) is delineated with black dashed lines for reference.

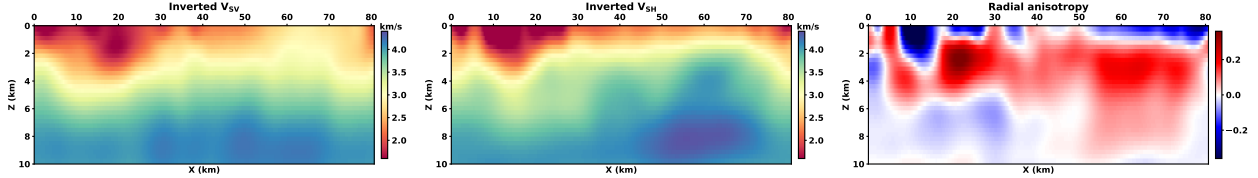


Figure 12: Inverted  $V_{SV}$  and  $V_{SH}$  for SB1 and the radial anisotropy, using data from 0.2 to 0.3 Hz. The same 1D initial model as in Figure 8a is used for both cases.

results from low frequencies (0.2 to 0.3 Hz) for comparison. The overall feature of the basin depth variation is captured in both inversions, while  $V_{SV}$  seems to penetrate deeper and  $V_{SH}$  provides better constraint for the shallower part. The radial anisotropy shows a clear sign flip along an interface that is likely to indicate changes in lithology. The near-surface negative anisotropy can result from vertical cracks caused by repeated earthquakes, which becomes positive with increasing depth and pressure due to the horizontal layering of sedimentary rocks (Jiang & Denolle, 2022). We are less convinced by the magnitude and depth resolution of the anisotropy and the reliability decreases with depth due to loss in sensitivity. It is important to note that the primary goal of this experiment, and indeed the entire study, is to demonstrate the functionality of a new, efficient, and generalized method rather than to delve into a detailed interpretation of any specific area. This is also why we chose a well-studied area, ensuring that we have results for validation.

## 5 Discussion

In this study, we have demonstrated the functionality of neural operators in realistic full waveform ambient noise inversion through a 2D case. Provided sufficient computational resources, the proposed method is expected to work in 3D without fundamental changes, while providing increased computational advantages over conventional methods. We aim to provide some plug-and-play models pre-trained to high accuracy for the community to apply to other regions on Earth. Because our model is trained within the framework of supervised learning, the fundamental assumption is that training and testing data follow the same distribution. Therefore, the model predictions are expected to fail where the velocity parameters deviate significantly from the training distribution. We show the training distributions of  $V_P$  and  $V_S$  associated with depth in Figure 13, allowing users to decide whether to directly use our model or perform additional training. Even in cases where re-training is necessary, a pre-trained model enables transfer learning that can greatly improve learning efficiency (Yosinski et al., 2014). Another aspect is that the model is not expected to extrapolate to larger physical domains than which it was trained on (80 km length by 40 km depth) or to frequencies outside the preset band of interest.

In performing FWI, we use gradient descent with AD instead of training a reverse model that directly maps from observed waveforms to velocity parameters. Although such end-to-end approaches are even faster (Moseley et al., 2020; Wu & Lin, 2019), they provide only a single solution without supervision on the data misfit. Such approaches are arguably not ideal for inverse problems because they are ill-posed and non-unique, unless they are combined with uncertainty quantification methods. We define the misfit function for inversion as the MSE in the frequency domain for convenient use with HNO, but it would be feasible and worthwhile to explore different misfit functions in either

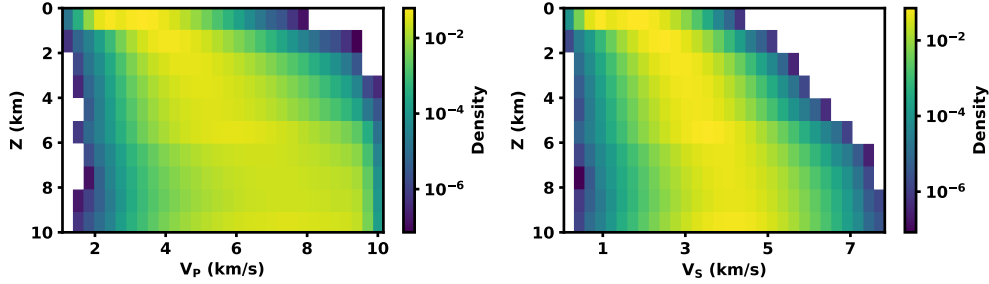


Figure 13: Training distributions of  $V_P$  and  $V_S$  associated with depth.

the frequency or time domain (Bozdağ et al., 2011; Métivier et al., 2018; Fournier & Oldenburg, 2019; Sambridge et al., 2022) to better tackle the non-uniqueness and cycle-skipping problems. However, the AD method requires a differentiable loss function, which is not compatible with, e.g., the cross-correlation time shift commonly used in FWI, unless some smooth approximation is applied.

The rapid developments in compute capabilities and machine learning research have positioned data-driven approaches as a promising new perspective on FWI. On one hand, data-driven approaches can greatly accelerate modeling and inversion while suffering less from typical gradient-based approximations in physics-driven approaches. On the other hand, they rely on data provided by physics-driven approaches and, therefore, will also benefit from any advancements in those approaches. In this study, we integrate these two types of approaches by first generating training data with a physics-driven solver and then training a data-driven model as a surrogate solver. Another way is to incorporate physics into the training loss, making it possible to remove the external solver (Li et al., 2024; Raissi et al., 2019; Rasht-Behesht et al., 2022; Ren et al., 2024; Song & Alkhalifah, 2021). While training with physics loss alone is challenging, combining it with a data loss has the potential to improve generalization ability and further benefit inversion.

## 6 Conclusions

We present the first application of neural operators in full waveform ambient noise inversion using several real seismic datasets from linear nodal arrays distributed across the northern LA basins. We show that a Helmholtz Neural Operator trained on random velocity fields can generalize to realistic velocity structures, while demonstrating robustness to random noise. In performing FWI with automatic differentiation, the neural operator is two orders of magnitude faster than the conventional SEM and does not require a separate adjoint source calculation. In comparison to the adjoint-state method relying on the Born approximation, our method has not linearized any gradients and is therefore less prone to cycle-skipping problems. The tomography results from real data align with multiple previous studies and can be obtained in a plug-and-play manner. We provide a trained model that can be directly applied to different regions, as long as the velocity parameters fall within the training distribution.

## Data Availability Statement

The node data can be accessed from the IRIS Data Management Center (BASIN, 2018), and the code, models, and processed data are available at [https://github.com/caifeng-zou/ANFWI\\_HNO](https://github.com/caifeng-zou/ANFWI_HNO) (Zou, 2025).

## Acknowledgements

ZER acknowledges financial support from the David and Lucile Packard Foundation.

## References

- Afanasiev, M., Boehm, C., van Driel, M., Krischer, L., Rietmann, M., May, D. A., Knepley, M. G., & Fichtner, A., 2019. Modular and flexible spectral-element waveform modelling in two and three dimensions, *Geophysical Journal International*, **216**(3), 1675–1692.
- Azizzadenesheli, K., Kovachki, N., Li, Z., Liu-Schiaffini, M., Kossaifi, J., & Anandkumar, A., 2024. Neural operators for accelerating scientific simulations and design, *Nature Reviews Physics*, **6**(5), 320–328.
- BASIN, 2018. San Gabriel and San Bernardino Basin Arrays, Dataset, doi:10.7909/46a0-ma59.
- Baydin, A. G., Pearlmutter, B. A., Radul, A. A., & Siskind, J. M., 2018. Automatic differentiation in machine learning: a survey, *Journal of machine learning research*, **18**(153), 1–43.
- Bensen, G., Ritzwoller, M., Barmin, M., Levshin, A. L., Lin, F., Moschetti, M., Shapiro, N., & Yang, Y., 2007. Processing seismic ambient noise data to obtain reliable broad-band surface wave dispersion measurements, *Geophysical journal international*, **169**(3), 1239–1260.
- Beydoun, W. B. & Tarantola, A., 1988. First Born and Rytov approximations: Modeling and inversion conditions in a canonical example, *The Journal of the Acoustical Society of America*, **83**(3), 1045–1055.
- Bozdağ, E., Trampert, J., & Tromp, J., 2011. Misfit functions for full waveform inversion based on instantaneous phase and envelope measurements, *Geophysical Journal International*, **185**(2), 845–870.
- Brocher, T. M., 2005. Empirical relations between elastic wavespeeds and density in the Earth’s crust, *Bulletin of the seismological Society of America*, **95**(6), 2081–2092.
- Chen, M., Huang, H., Yao, H., van der Hilst, R., & Niu, F., 2014. Low wave speed zones in the crust beneath SE Tibet revealed by ambient noise adjoint tomography, *Geophysical Research Letters*, **41**(2), 334–340.
- Clayton, R., Persaud, P., Denolle, M., & Polet, J., 2019. Exposing Los Angeles’s Shaky Geologic Underbelly (Vol. 100), *Eos*. <https://doi.org/10.1029>.
- Elliott, C., 2018. The simple essence of automatic differentiation, *Proceedings of the ACM on Programming Languages*, **2**(ICFP), 1–29.

- Fichtner, A., Bunge, H.-P., & Igel, H., 2006a. The adjoint method in seismology: I. Theory, *Physics of the Earth and Planetary Interiors*, **157**(1-2), 86–104.
- Fichtner, A., Bunge, H.-P., & Igel, H., 2006b. The adjoint method in seismology—: II. Applications: Traveltimes and sensitivity functionals, *Physics of the Earth and Planetary Interiors*, **157**(1-2), 105–123.
- Forbriger, T., Groos, L., & Schäfer, M., 2014. Line-source simulation for shallow-seismic data. Part 1: theoretical background, *Geophysical Journal International*, **198**(3), 1387–1404.
- Fournier, D. & Oldenburg, D. W., 2019. Inversion using spatially variable mixed Lp norms, *Geophysical Journal International*, **218**(1), 268–282.
- Gauthier, O., Virieux, J., & Tarantola, A., 1986. Two-dimensional nonlinear inversion of seismic waveforms: Numerical results, *geophysics*, **51**(7), 1387–1403.
- Ghose, R., Persaud, P., & Clayton, R. W., 2023. Basin Structure for Earthquake Ground Motion Estimates in Urban Los Angeles Mapped with Nodal Receiver Functions, *Geosciences*, **13**(11), 320.
- Guo, Z., Chen, Y. J., Ning, J., Feng, Y., Grand, S. P., Niu, F., Kawakatsu, H., Tanaka, S., Obayashi, M., & Ni, J., 2015. High resolution 3-D crustal structure beneath NE China from joint inversion of ambient noise and receiver functions using NECESSArray data, *Earth and Planetary Science Letters*, **416**, 1–11.
- Hendrycks, D. & Gimpel, K., 2016. Gaussian error linear units (gelus), *arXiv preprint arXiv:1606.08415*.
- Hornik, K., Stinchcombe, M., & White, H., 1989. Multilayer feedforward networks are universal approximators, *Neural networks*, **2**(5), 359–366.
- Hudson, J. et al., 1977. Scattered waves in the coda of P, *Journal of Geophysics*, **43**(1), 359–374.
- Jaxybulatov, K., Shapiro, N., Koulakov, I., Mordret, A., Landès, M., & Sens-Schönfelder, C., 2014. A large magmatic sill complex beneath the Toba caldera, *science*, **346**(6209), 617–619.
- Jiang, C. & Denolle, M. A., 2022. Pronounced seismic anisotropy in Kanto sedimentary basin: A case study of using dense arrays, ambient noise seismology, and multi-modal surface-wave imaging, *Journal of Geophysical Research: Solid Earth*, **127**(8), e2022JB024613.
- Kingma, D. P. & Ba, J., 2014. Adam: A method for stochastic optimization, *arXiv preprint arXiv:1412.6980*.
- Kovachki, N. B., Li, Z., Liu, B., Azizzadenesheli, K., Bhattacharya, K., Stuart, A. M., & Anandkumar, A., 2023. Neural Operator: Learning Maps Between Function Spaces With Applications to PDEs., *J. Mach. Learn. Res.*, **24**(89), 1–97.
- Lee, E.-J., Chen, P., Jordan, T. H., Maechling, P. B., Denolle, M. A., & Beroza, G. C., 2014. Full-3-D tomography for crustal structure in southern California based on the scattering-integral and the adjoint-wavefield methods, *Journal of Geophysical Research: Solid Earth*, **119**(8), 6421–6451.

- Li, Y., Villa, V., Clayton, R. W., & Persaud, P., 2023. Shear Wave Velocities in the San Gabriel and San Bernardino Basins, California, *Journal of Geophysical Research: Solid Earth*, **128**(7), e2023JB026488.
- Li, Z., Kovachki, N., Azizzadenesheli, K., Liu, B., Bhattacharya, K., Stuart, A., & Anandkumar, A., 2020a. Fourier neural operator for parametric partial differential equations, *arXiv preprint arXiv:2010.08895*.
- Li, Z., Kovachki, N., Azizzadenesheli, K., Liu, B., Bhattacharya, K., Stuart, A., & Anandkumar, A., 2020b. Neural operator: Graph kernel network for partial differential equations, *arXiv preprint arXiv:2003.03485*.
- Li, Z., Kovachki, N., Azizzadenesheli, K., Liu, B., Stuart, A., Bhattacharya, K., & Anandkumar, A., 2020c. Multipole graph neural operator for parametric partial differential equations, *Advances in Neural Information Processing Systems*, **33**, 6755–6766.
- Li, Z., Zheng, H., Kovachki, N., Jin, D., Chen, H., Liu, B., Azizzadenesheli, K., & Anandkumar, A., 2024. Physics-informed neural operator for learning partial differential equations, *ACM/JMS Journal of Data Science*, **1**(3), 1–27.
- Lin, F.-C., Moschetti, M. P., & Ritzwoller, M. H., 2008. Surface wave tomography of the western United States from ambient seismic noise: Rayleigh and Love wave phase velocity maps, *Geophysical Journal International*, **173**(1), 281–298.
- Liu, Q. & Tromp, J., 2006. Finite-frequency kernels based on adjoint methods, *Bulletin of the Seismological Society of America*, **96**(6), 2383–2397.
- Liu, X., Beroza, G. C., & Li, H., 2023. Ambient noise differential adjoint tomography reveals fluid-bearing rocks near active faults in Los Angeles, *Nature Communications*, **14**(1), 6873.
- Liu, Y., Niu, F., Chen, M., & Yang, W., 2017. 3-D crustal and uppermost mantle structure beneath NE China revealed by ambient noise adjoint tomography, *Earth and Planetary Science Letters*, **461**, 20–29.
- Louboutin, M., Lange, M., Luporini, F., Kukreja, N., Witte, P. A., Herrmann, F. J., Velesko, P., & Gorman, G. J., 2019. Devito (v3.1.0): an embedded domain-specific language for finite differences and geophysical exploration, *Geoscientific Model Development*, **12**(3), 1165–1187.
- Maguire, R., Schmandt, B., Li, J., Jiang, C., Li, G., Wilgus, J., & Chen, M., 2022. Magma accumulation at depths of prior rhyolite storage beneath Yellowstone Caldera, *Science*, **378**(6623), 1001–1004.
- Métivier, L., Allain, A., Brossier, R., Méridot, Q., Oudet, E., & Virieux, J., 2018. Optimal transport for mitigating cycle skipping in full-waveform inversion: A graph-space transform approach, *Geophysics*, **83**(5), R515–R540.
- Miles, J. W., 1960. Scattering of elastic waves by small inhomogeneities, *Geophysics*, **25**(3), 642–648.
- Moseley, B., Nissen-Meyer, T., & Markham, A., 2020. Deep learning for fast simulation of seismic waves in complex media, *Solid Earth*, **11**(4), 1527–1549.

- Panning, M. P., Capdeville, Y., & Romanowicz, B. A., 2009. Seismic waveform modelling in a 3-D Earth using the Born approximation: potential shortcomings and a remedy, *Geophysical Journal International*, **177**(1), 161–178.
- Pladys, A., Brossier, R., Li, Y., & Métivier, L., 2021. On cycle-skipping and misfit function modification for full-wave inversion: Comparison of five recent approaches, *Geophysics*, **86**(4), R563–R587.
- Plessix, R.-E., 2006. A review of the adjoint-state method for computing the gradient of a functional with geophysical applications, *Geophysical Journal International*, **167**(2), 495–503.
- Rahman, M. A., Ross, Z. E., & Azizzadenesheli, K., 2022. U-NO: U-shaped neural operators, *arXiv preprint arXiv:2204.11127*.
- Raissi, M., Perdikaris, P., & Karniadakis, G. E., 2019. Physics-informed neural networks: A deep learning framework for solving forward and inverse problems involving nonlinear partial differential equations, *Journal of Computational physics*, **378**, 686–707.
- Rasht-Behesht, M., Huber, C., Shukla, K., & Karniadakis, G. E., 2022. Physics-informed neural networks (PINNs) for wave propagation and full waveform inversions, *Journal of Geophysical Research: Solid Earth*, **127**(5), e2021JB023120.
- Ren, P., Rao, C., Chen, S., Wang, J.-X., Sun, H., & Liu, Y., 2024. SeismicNet: Physics-informed neural networks for seismic wave modeling in semi-infinite domain, *Computer Physics Communications*, **295**, 109010.
- Ronneberger, O., Fischer, P., & Brox, T., 2015. U-net: Convolutional networks for biomedical image segmentation, in *Medical Image Computing and Computer-Assisted Intervention—MICCAI 2015: 18th International Conference, Munich, Germany, October 5–9, 2015, Proceedings, Part III 18*, pp. 234–241, Springer.
- Rumelhart, D. E., Hinton, G. E., & Williams, R. J., 1986. Learning representations by back-propagating errors, *nature*, **323**(6088), 533–536.
- Sager, K., Ermert, L., Boehm, C., & Fichtner, A., 2018. Towards full waveform ambient noise inversion, *Geophysical Journal International*, **212**(1), 566–590.
- Sager, K., Boehm, C., Ermert, L., Krischer, L., & Fichtner, A., 2020. Global-scale full-waveform ambient noise inversion, *Journal of Geophysical Research: Solid Earth*, **125**(4), e2019JB018644.
- Sambridge, M., Jackson, A., & Valentine, A. P., 2022. Geophysical inversion and optimal transport, *Geophysical Journal International*, **231**(1), 172–198.
- Schäfer, M., Groos, L., Forbriger, T., & Bohlen, T., 2014. Line-source simulation for shallow-seismic data. Part 2: full-waveform inversion—a synthetic 2-D case study, *Geophysical Journal International*, **198**(3), 1405–1418.
- Song, C. & Alkhalifah, T. A., 2021. Wavefield reconstruction inversion via physics-informed neural networks, *IEEE Transactions on Geoscience and Remote Sensing*, **60**, 1–12.

- Tape, C., Liu, Q., Maggi, A., & Tromp, J., 2010. Seismic tomography of the southern California crust based on spectral-element and adjoint methods, *Geophysical Journal International*, **180**(1), 433–462.
- Tromp, J., Tape, C., & Liu, Q., 2005. Seismic tomography, adjoint methods, time reversal and banana-doughnut kernels, *Geophysical Journal International*, **160**(1), 195–216.
- Tromp, J., Luo, Y., Hanasoge, S., & Peter, D., 2010. Noise cross-correlation sensitivity kernels, *Geophysical Journal International*, **183**(2), 791–819.
- Tsai, V. C., Sager, K., & Bowden, D. C., 2024. Towards limited-domain full waveform ambient noise inversion, *Geophysical Journal International*, **237**(2), 965–973.
- Villa, V., Li, Y., Clayton, R. W., & Persaud, P., 2023. Three-Dimensional Basin Depth Map of the Northern Los Angeles Basins From Gravity and Seismic Measurements, *Journal of Geophysical Research: Solid Earth*, **128**(7), e2022JB025425.
- Virieux, J. & Operto, S., 2009. An overview of full-waveform inversion in exploration geophysics, *Geophysics*, **74**(6), WCC1–WCC26.
- Wang, K., Yang, Y., Basini, P., Tong, P., Tape, C., & Liu, Q., 2018. Refined crustal and uppermost mantle structure of southern California by ambient noise adjoint tomography, *Geophysical Journal International*, **215**(2), 844–863.
- Wang, K., Yang, Y., Jiang, C., Wang, Y., Tong, P., Liu, T., & Liu, Q., 2021. Adjoint tomography of ambient noise data and teleseismic P waves: Methodology and applications to central California, *Journal of Geophysical Research: Solid Earth*, **126**(6), e2021JB021648.
- Wapenaar, K., 2004. Retrieving the Elastodynamic Green’s Function of an Arbitrary Inhomogeneous Medium by Cross Correlation, *Physical review letters*, **93**(25), 254301.
- Wapenaar, K., Slob, E., Snieder, R., & Curtis, A., 2010. Tutorial on seismic interferometry: Part 2—Underlying theory and new advances, *Geophysics*, **75**(5), 75A211–75A227.
- Wright, T. L., 1991. Structural geology and tectonic evolution of the Los Angeles basin, California, in *Active Margin Basins*, vol. 52 of **AAPG Memoir**, pp. 35–79, ed. Biddle, K. T., American Association of Petroleum Geologists.
- Wu, R.-S. & Aki, K., 1985. Scattering characteristics of elastic waves by an elastic heterogeneity, *Geophysics*, **50**(4), 582–595.
- Wu, S., Yao, J., Wei, S., Hubbard, J., Wang, Y., Htwe, Y. M. M., Thant, M., Wang, X., Wang, K., Liu, T., et al., 2021. New insights into the structural heterogeneity and geodynamics of the Indo-Burma subduction zone from ambient noise tomography, *Earth and Planetary Science Letters*, **562**, 116856.
- Wu, Y. & Lin, Y., 2019. InversionNet: An efficient and accurate data-driven full waveform inversion, *IEEE Transactions on Computational Imaging*, **6**, 419–433.
- Yang, Y., Gao, A. F., Castellanos, J. C., Ross, Z. E., Azizzadenesheli, K., & Clayton, R. W., 2021. Seismic wave propagation and inversion with neural operators, *The Seismic Record*, **1**(3), 126–134.

- Yang, Y., Gao, A. F., Azizzadenesheli, K., Clayton, R. W., & Ross, Z. E., 2023. Rapid seismic waveform modeling and inversion with neural operators, *IEEE Transactions on Geoscience and Remote Sensing*, **61**, 1–12.
- Yao, G., da Silva, N. V., Warner, M., Wu, D., & Yang, C., 2019. Tackling cycle skipping in full-waveform inversion with intermediate data, *Geophysics*, **84**(3), R411–R427.
- Yao, H., van Der Hilst, R. D., & De Hoop, M. V., 2006. Surface-wave array tomography in SE Tibet from ambient seismic noise and two-station analysis—I. Phase velocity maps, *Geophysical Journal International*, **166**(2), 732–744.
- Yao, H., van Der Hilst, R. D., & Montagner, J.-P., 2010. Heterogeneity and anisotropy of the lithosphere of SE Tibet from surface wave array tomography, *Journal of Geophysical Research: Solid Earth*, **115**(B12).
- Yosinski, J., Clune, J., Bengio, Y., & Lipson, H., 2014. How transferable are features in deep neural networks?, *Advances in neural information processing systems*, **27**.
- Zhang, C., Yao, H., Liu, Q., Zhang, P., Yuan, Y. O., Feng, J., & Fang, L., 2018. Linear array ambient noise adjoint tomography reveals intense crust-mantle interactions in North China Craton, *Journal of Geophysical Research: Solid Earth*, **123**(1), 368–383.
- Zheng, Y., Shen, W., Zhou, L., Yang, Y., Xie, Z., & Ritzwoller, M. H., 2011. Crust and uppermost mantle beneath the North China Craton, northeastern China, and the Sea of Japan from ambient noise tomography, *Journal of Geophysical Research: Solid Earth*, **116**(B12).
- Zhu, H., Bozdağ, E., & Tromp, J., 2015. Seismic structure of the European upper mantle based on adjoint tomography, *Geophysical Journal International*, **201**(1), 18–52.
- Zou, C., 2025. caifeng-zou/ANFWI\_HNO: First release, Software.
- Zou, C. & Clayton, R. W., 2024. Imaging the Northern Los Angeles Basins with Autocorrelations, *Seismological Research Letters*.
- Zou, C., Azizzadenesheli, K., Ross, Z. E., & Clayton, R. W., 2024. Deep neural Helmholtz operators for 3-D elastic wave propagation and inversion, *Geophysical Journal International*, **239**(3), 1469–1484.

## Supplementary Materials

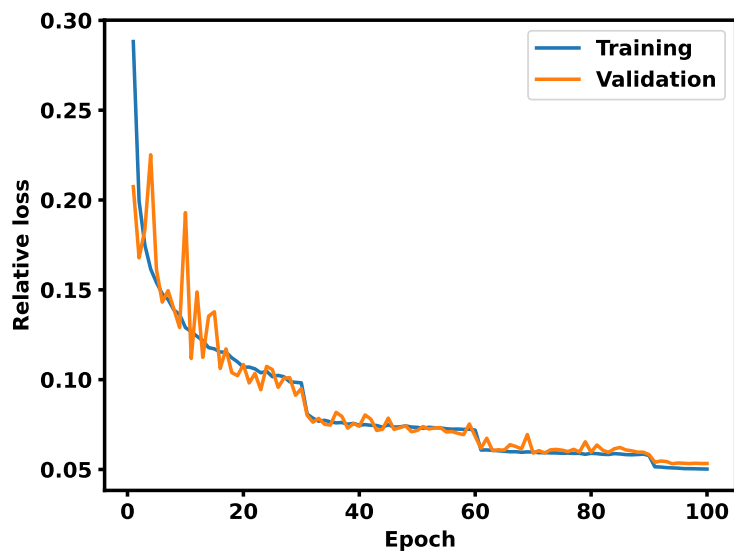


Figure S1: Loss curves. The batch size is 256. We use an Adam optimizer with a learning rate of 0.001 and a scheduler that decays the learning rate by half every 30 epochs.

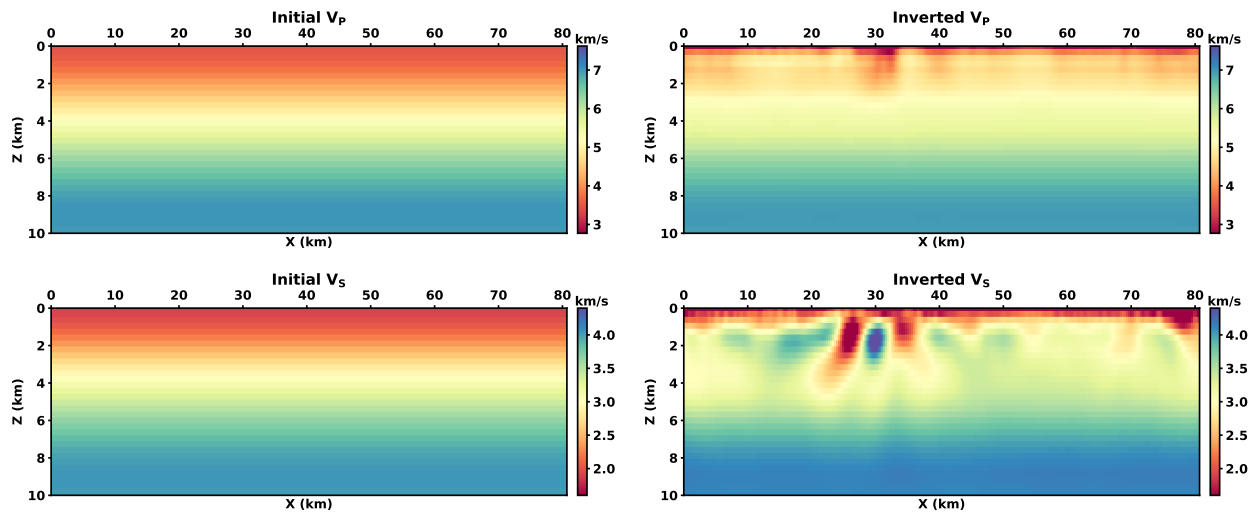


Figure S2: FWI results for noise-free data using the adjoint-state method with the same 1D initialization as in Figure 5.

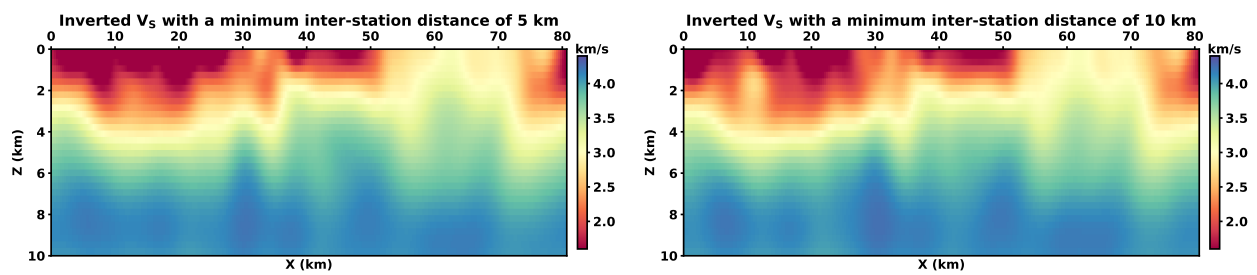


Figure S3: Inverted  $V_s$  for SB1 with minimum inter-station distances of 5 km (Figure 8a) and 10 km.

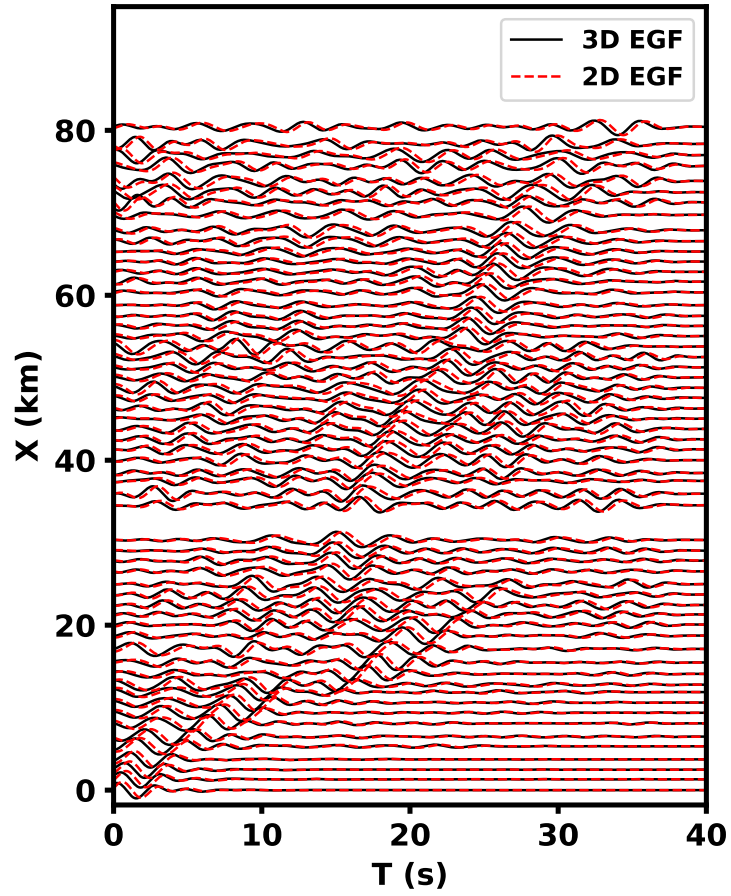


Figure S4: 3-to-2D converted EGF created from ambient noise cross-correlation for SB1. Every fourth trace is displayed.

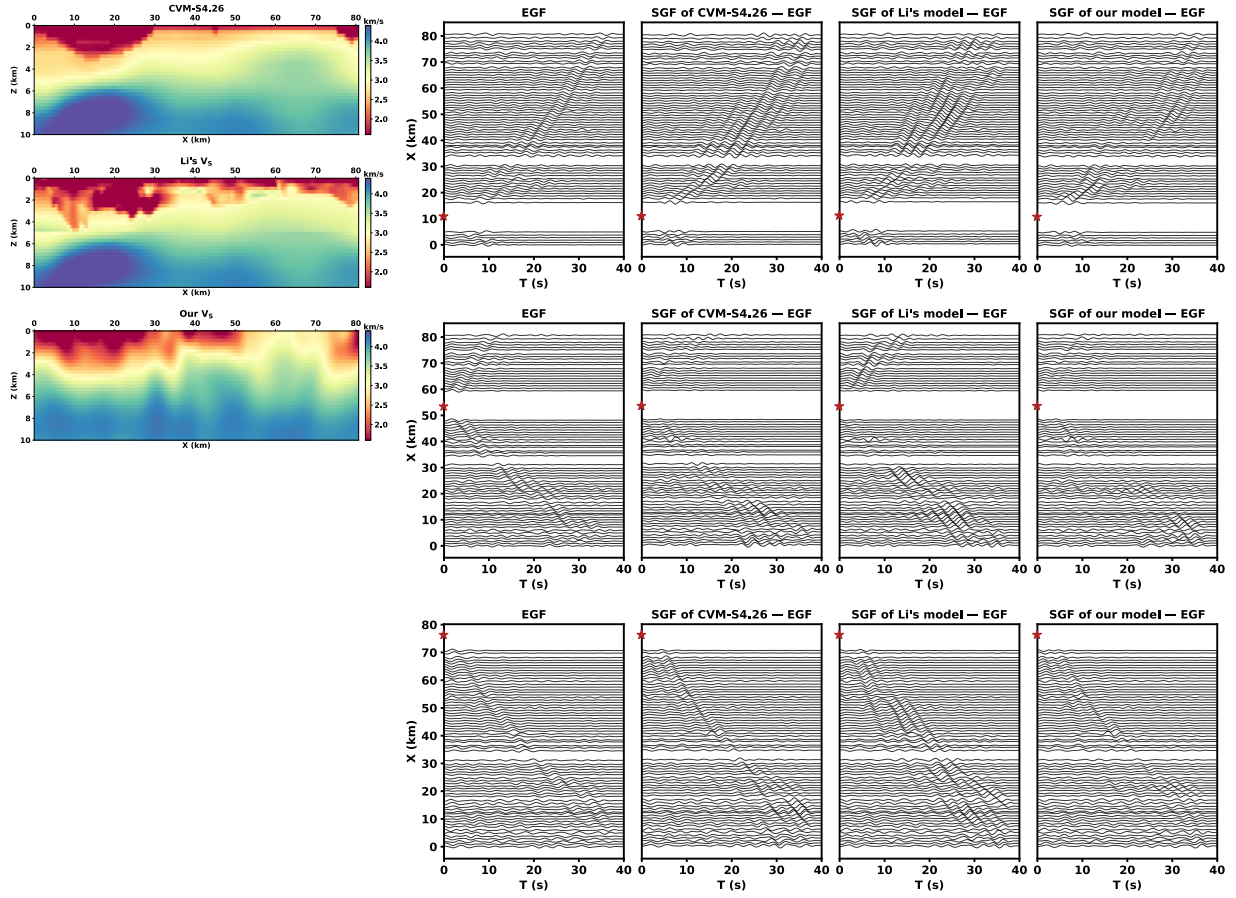


Figure S5: Waveform difference plots corresponding to Figure 9.

Table S1: Details in each FNO layer.

Layer	Input co-dimension	Output co-dimension	Dimension	Number of modes	Activation
1	32 (lifting dimension)	64	(192, 96)	(96, 48)	GELU
2	64	128	(128, 64)	(64, 32)	GELU
3	128	256	(64, 32)	(32, 16)	GELU
4	256	512	(32, 16)	(16, 8)	GELU
5	512	256	(64, 32)	(16, 8)	GELU
6	512	128	(128, 64)	(32, 16)	GELU
7	256	64	(192, 96)	(64, 32)	GELU
8	128	64	(256, 128)	(96, 48)	GELU

Table S2: Parameters for the random fields used to generate velocity models.

Velocity model	Covariance	$var$	$len\_scale$	$nu$	Background
$V_S = BG_S \times (1 + RF_S/100)$	$RF_S$ : Matérn	400	(64, 8)	1.5	$BG_S$ : 1D from Lee et al. (2014)
$V_P = BG_P \times (1 + RF_P/100)$	$RF_P$ : Matérn	4	(64, 8)	2.5	$BG_P(V_S)$ : Brocher (2005)